Observation of recollision-based high-harmonic generation in liquid isopropanol and the role of electron scattering

Oliver Alexander, Jonathan C. T. Barnard, Esben W. Larsen [*], Timur Avni [†], Sebastian Jarosch,
Clément Ferchaud, Andrew Gregory, Susan Parker, Gediminas Galinis, Alexandra Tofful, Douglas Garratt,
Mary R. Matthews [‡], and Jonathan P. Marangos

Quantum Optics and Laser Science Group, Blackett Laboratory, Imperial College London, London SW7 2BW, United Kingdom

We report extreme-ultraviolet high-harmonic generation (HHG) from liquid isopropanol, extending up to 50 eV, when using 1800-nm carrier envelope phase stable pulses of 1.8 cycles with intensities below the laser breakdown threshold. We study the mechanism of the harmonic emission through its dependence on the driving field and find it to be consistent with a strong-field recombination mechanism. We explore the role of scattering from neighboring molecules in simulations using empirical cross-section data. We find that these simulations, within a full propagation calculation, provide good quantitative agreement with the measured intensity-dependent harmonic cutoffs and demonstrate that HHG emission in the liquid phase can be used to corroborate ultrafast electron-scattering processes.

I. INTRODUCTION

Bright coherent high-harmonic generation (HHG) is a universal phenomenon observed when a strong laser field interacts with matter. It has been observed in all common phases of matter (plasmas, gases, solids, and liquids). In gases this method is widely used for producing attosecond extreme-ultraviolet (EUV) pulses [1,2] for studying the structure and dynamics of matter at electronic timescales [3–5]. In solids the observation of nonperturbative harmonic emission from ultrashort laser pulses [6] sparked a wave of studies [7,8] as a probe of charge carrier dynamics under strong fields and a route to EUV attosecond photonic devices [9]. For liquids, high-harmonic generation [10–12] is far less well explored, and the mechanism behind HHG in the liquid phase is hitherto not understood. This is partly due to the challenges of detecting EUV emission from thick and absorbing cylindrical jets or spherical droplets. Nonperturbative harmonics [12] generated in the liquid phase were made possible with new technology for optically flat and thin sheets of liquid [13,14].

A. HHG in the gas phase

A real-space recombination picture is useful in understanding HHG: A strong laser field distorts the atomic and molecular potential or band structure of the material [15], and electron wave packets, formed by tunneling through the distorted potentials, are accelerated and returned by the oscillating field to the hole state. In atomic gases the accrued kinetic energy is converted into high-energy photons ranging from EUV to soft x-ray energies. The highest achievable photon energy in this case, $\hbar\omega_{max}$, can be estimated with the classical cutoff law: $\hbar\omega_{max} = I_p + 3.17U_p$, where I_p and U_p are the ionization potential and ponderomotive energy, respectively. This manifests in a theoretical cutoff energy which is linear with intensity. This is limited in experiments by ionization saturation which distorts the driving laser beam, e.g., intensities of the order of 10^{14} W cm^{-2} at 800 nm, by over-the-barrier ionization, and by phase-matching considerations across the interaction region.

B. HHG in the condensed phase

In solids, a reciprocal-space picture can be used to describe strong-field-driven electron dynamics with a recombination component occurring between electronic bands (interband component) and an additional nonlinear intraband component. Both complementary processes give cutoff energies which are linear with the electric field amplitude, governed by the nonparabolic electron energy-momentum dispersion within a band structure. This theoretical cutoff becomes limited by the combined phase-matching, absorption, and damage threshold of the solid at the applied laser pulse duration and wavelength. In more recent studies, real-space descriptions have been employed as they provide physical insight into scattering phenomena [16,17], spatial structure, delocalization, and coherent recombination [18,19].

Higher-order harmonics in the liquid phase were first observed using 150-μm-thick films of H_2O and D_2O by DiChiara *et al.* [11], with up to the 13th harmonic observed above a saturation intensity, but not directly attributed to a nonperturbative effect. Work by Kurz *et al.* [10] reported

---

[*]Present address: IMEC, Kapeldreef 75, 3001 Leuven, Belgium.

[†]Present address: Central Laser Facility, Harlow Campus, Didcot OX11 0QX, United Kingdom.

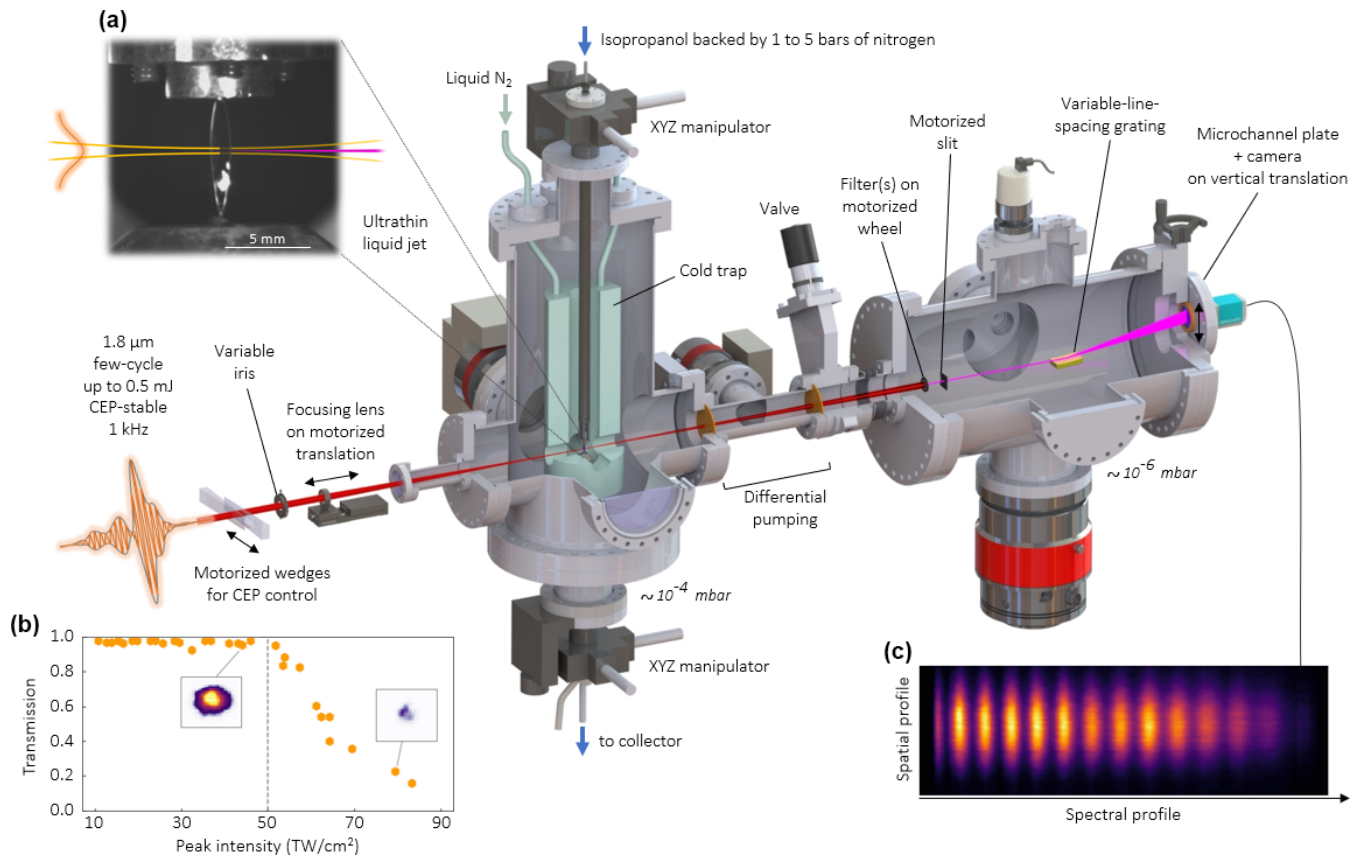[‡]Corresponding author: m.matthews@imperial.ac.uk

FIG. 1. Overview of the experimental setup. (a) In-vacuum image of the liquid jet sheet, with the laser beam position indicated. (b) Laser beam transmission through the liquid sheet with increasing intensity. Transmission drops rapidly after 53 TW cm^{-2}. Insets: images of the driving beam, after the liquid sheet, at intensities below and above the breakdown threshold. (c) Example of spatial-spectral profile of harmonics generated in liquid phase isopropanol.

nonperturbative high-order harmonics from vaporized water droplets where the harmonic yield was subsequently quenched above a threshold vapor density, while Luu *et al.* [12] observed nonperturbative harmonics from a liquid sheet with a cutoff of 25 eV (34th harmonic order) and a linear scaling of the cutoff with electric field amplitude. A recent theoretical study has proposed an explanation for the deviation from the strong-field recombination behavior based on the effects of increased disorder on the electron recombination probability [20]. There is as yet no consensus on the correct theoretical framework with which to view liquid phase HHG, and further new experimental data are important for this research to progress.

We explore EUV emission from liquid isopropanol in a vacuum under illumination of a longer-wavelength driving field with pulses ranging between 1.8 and 2.5 cycles, examining the behavior of the emission with varied intensity and carrier envelope phase (CEP). We find that the shortest possible pulse produces the highest-energy emission of 50 eV, when using a CEP-stable, 1.8-cycle driving field with an intensity maintained below the liquid damage threshold, reducing to 45 eV for longer (2.2 cycle) pulses. We also observe that too high an intensity can have a detrimental effect on the cutoff energy, observing a 35-eV cutoff at intensities above the damage threshold. Above the liquid damage threshold, in the overdriven regime, plasma reflection and ionization saturation effects clamp the intensity, distort the driving pulse,

and reduce drastically the harmonics flux [21]. Studies of harmonic generation in dense water vapor [10] showed that an increasing vapor density led to a decreasing cutoff energy, and this was attributed to increasing electron-scattering rates. Similarly, below the liquid damage threshold, we find evidence that electron scattering plays a significant role and that, when incorporated into a recombination model, it introduces a deviation from the classical cutoff law. We show that a modification to gas phase electron-molecule scattering cross sections to take into account the effects of screening, correlation, and exchange potentials (expected in dense molecular environments [22–24]) is able to capture accurately the contribution of scattering to HHG in liquids. Our findings support the use of a real-space collision picture, modified to account for electron scattering, in order to describe the mechanism of HHG in a liquid.

II. EXPERIMENT

A. Illumination of a liquid jet with few-cycle pulses below the damage threshold

The experiment was carried out using a thin ($\sim$1.5 µm) flat sheet of liquid isopropanol [13,25] illuminated with 1.8-µm pulses (Fig. 1) ranging in duration from 11 to 15 fs. These few-cycle pulses, i.e., 1.8–2.5 cycles, are CEP controlled, linearly polarized, and range from 100 to 350 µJ energy. They are

focused into a thin sheet of liquid running in a vacuum (10^{-4} mbar). The intensity-dependent laser transmission through the jet is shown in Fig. 1(b). This shows that up to a threshold intensity of 53 TW cm^{-2} the laser propagates through the liquid without significant loss, but that above this intensity threshold there is an abrupt reduction of the transmission. This reduction is caused by overionization of the liquid where the electron density exceeds the critical density for this wavelength, leading to a strong reflection of the laser at the front surface and a clamping of the intensity entering into the liquid [21]. It also coincides with the appearance of a vapor plume at the front surface of the jet [21]. It is important to note that the plasma density is dependent on the temporal properties of the driving laser as well as the peak intensity. A longer pulse of the same peak intensity will result in a larger plasma density buildup and is expected to break down before the 53 TW cm^{-2} threshold intensity we observed [21,26,27]. Therefore the use of few-cycle pulses allows us to operate at higher intensities while remaining below the damage threshold of the material. Our systematic studies of the mechanism of HHG from the liquid are confined to intensities below this damage threshold.

The liquid sheet is produced using a home-built fan-spray nozzle, presented in Ref. [13]. This nozzle (in contrast to a free-space [14] or chip-based [28] colliding-jets nozzle) produces a thin sheet by squeezing an expanding stream of liquid through a rectangular slit, transforming transverse momentum components into momentum in the plane of the slit. This approach damps the vibrations that arise due to this change in momentum, leading to a flatter sheet, which is important for avoiding spatial distortions in the generated harmonics. It also produces sheets which are thicker than colliding geometries. Our target is ~1.5 µm thick, i.e., similar to the wavelength of the driving field. We discuss these targets and compare their physical properties with those of chip-based liquid targets in Ref. [25]. No systematic studies exist which compare the surrounding vapor pressure of different liquid targets, but we anticipate that this is similar. Harmonic emission is detected on a flat-field EUV spectrometer consisting of a filter, slit, variable-line-spacing grating, microchannel plate, and camera. Figure 1(c) shows an example of typical harmonic emission collected on the detector, with the distribution of the harmonics on one axis and the spectral information on the
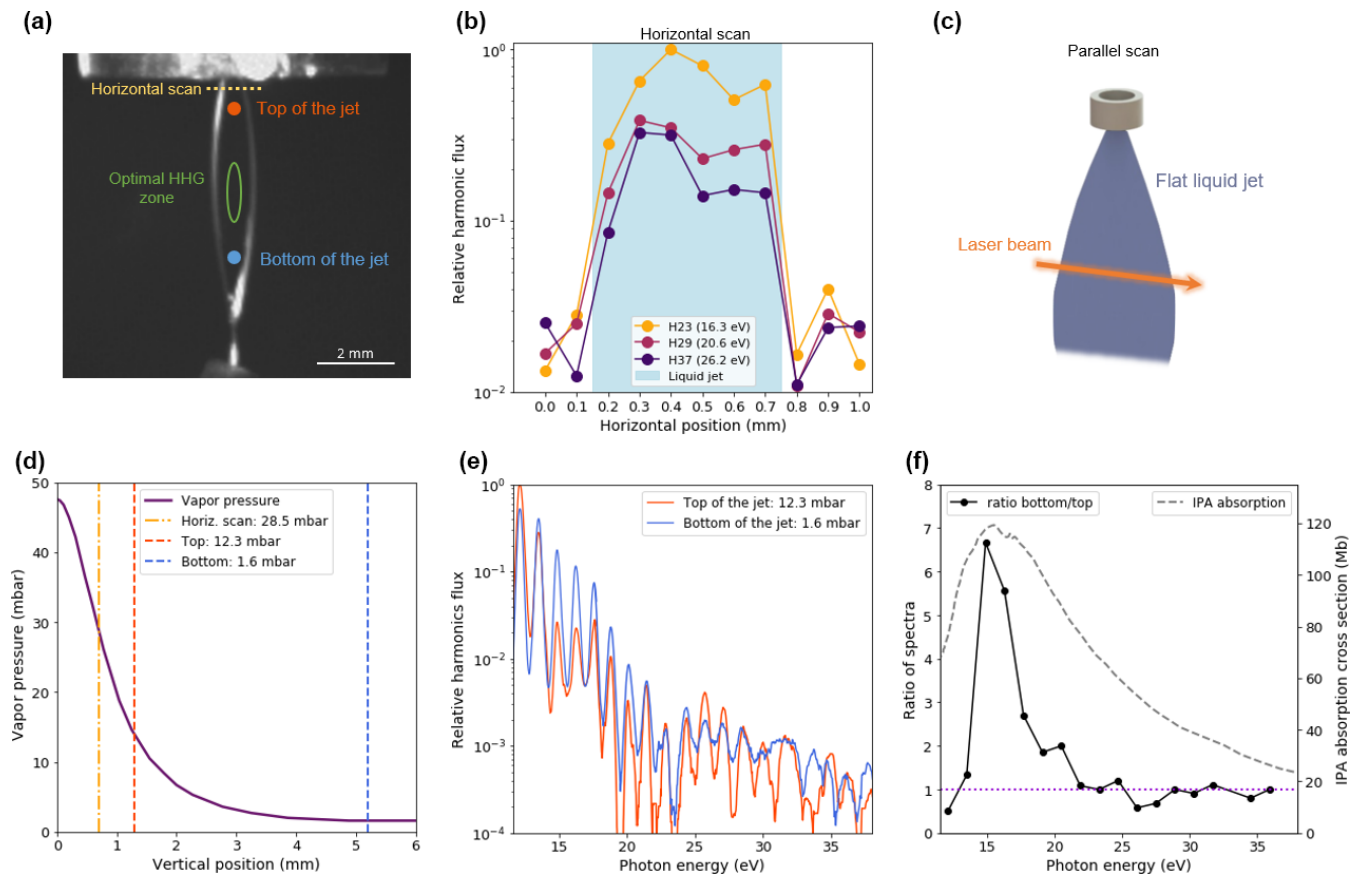

FIG. 2. (a) Front view of the liquid sheet showing regions where harmonic spectra were taken, i.e., a horizontal scan across the face and scans at the top and bottom of the sheet. (b) Horizontal scan of the flux of three harmonics recorded in 11 steps of 100 µm across the sheet. Sharp drops in harmonic yield are visible at the boundaries. No signal is observed on either side of the liquid. (c) To isolate possible emission from the surrounding vapor, the liquid sheet is rotated parallel and close to the laser axis. (d) Change in isopropanol vapor pressure with height along the sheet due to evaporative cooling. Dashed and dash-dotted lines show the scan heights. Horiz., horizontal. (e) Harmonic scans at the top and bottom of the liquid sheet, passing through different vapor densities and experiencing different absorption. (f) Solid line, ratio of spectra taken in (e); dashed line, isopropanol (IPA) absorption cross section from Ref. [29]. The difference in spectral intensity at 15 eV is due to increased absorption from the higher vapor pressure at the top of the jet. The dotted line is a guide to the eye. Cross sections are shown in megabarns (1 Mb = 10^{-22} cm^2).

other. The position of the camera could be adjusted to view different regions of the spectrum.

B. Validation of EUV emission from liquid phase

Due to evaporative cooling, the gas density (vapor pressure) at the surface of the jet is reduced from 1.2×10^{18} cm^{-3} (48 mbar) at the nozzle exit to 4×10^{16} cm^{-3} (<2 mbar) at the end of the first liquid sheet [Figs. 2(a) and 2(d)]. Although the density rapidly decreases away from the jet, decaying over a few hundred micrometers [25], this vapor absorbs EUV emission generated in the liquid and could potentially be an additional source of HHG emission. To quantify this, a horizontal scan of the liquid target relative to the interaction point was performed across the upper region of the jet [Figs. 2(a) and 2(b)], where the isopropanol number density is 7×10^{17} cm^{-3} (28 mbar). To identify the position on the jet, the intensity of the driving field was set to $\sim$80 TW cm^{-2} so that a plume is clearly visible, i.e., above the threshold, for this particular purpose. The harmonic spectral flux shows a distinct top-hat emission pattern corresponding to the physical size of the jet, with no emission detected when passing only through the vapor on either side of the jet edge [Fig. 2(b)]. This was confirmed by rotating the jet sheet about the vertical axis and allowing the laser pulses to pass parallel to the sides of the jet, a couple of hundred micrometers from the liquid surface [Fig. 2(c)]. HHG emission was observed in this configuration only above 170 TW cm^{-2}, more than three times the maximum intensity used in this paper (see Appendixes). In the center of the jet, where we took the remainder of the data, the number density was $<1 \times 10^{17}$ cm^{-3}, one or two orders of magnitude lower than is typically necessary for gas phase HHG from organic molecules [30].

Furthermore, when comparing harmonics spectra taken at the top and bottom of the jet in Fig. 2(e), where the vapor pressures are 12.3 and 1.6 mbar, respectively, we do not observe a significant modification to the overall harmonic flux. This is despite the vapor number density varying by an order of magnitude. Only in the region around 15 eV, in the case of the top of the jet (red curve), where there is a peak in the absorption of isopropanol, is there a change. This is due to increased reabsorption of the harmonics generated from the liquid by the higher vapor pressure or gas density found at the top of the jet [Figs. 2(e) and 2(f)]. This is highlighted in Fig. 2(f), which shows the ratio between the spectrum taken from the top of the jet and the spectrum taken from the bottom.

In summary, we carefully constrain the isopropanol vapor production in four ways: (1) through the correct choice of the position on the jet where there is low vapor pressure, (2) by preventing plasma explosions from the jet with every shot through the use of lower and carefully calibrated intensities, (3) by using a fan-spray nozzle where the collision occurs in the nozzle interior, not in the vacuum, thereby limiting splashing and vapor production from the precursor cylindrical jets, and (4) with a liquid-nitrogen-filled cold trap surrounding the jet (cold surface, 0.17 m^2). We can conclude that under the conditions of our experiment, at a lower intensity where no vapor plume is observed and with a sufficiently low surrounding vapor pressure, the observed harmonics are generated in the liquid with a negligible contribution from the gas. Figure 2(e) shows the four orders of magnitude of harmonic
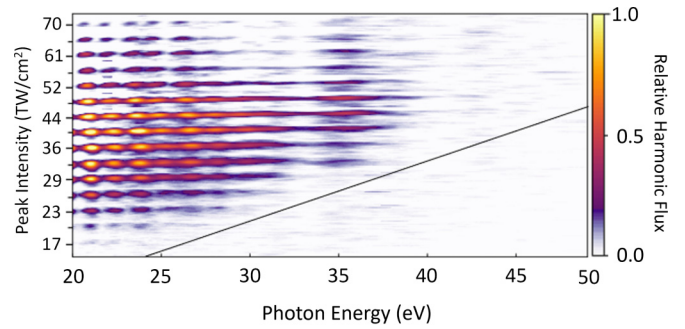

FIG. 3. Stacked microchannel plate (MCP) images at increasing intensities, varied using an iris. Each image show the spatial divergence in the y axis, with the discretized y axis marking the peak intensity used for the image acquisition. Black line, classical cutoff law of the three-step model. The pulse duration is 13 fs (2.2 cycles).

signal which are observable with our detection system in a low-vapor regime.

III. RESULTS

Figure 3 shows the evolution of higher-energy harmonics driven by a 2.2-cycle pulse, extending here to 45 eV, with increasing pump intensity. We observe a higher cutoff than previous works, as we work below the breakdown threshold with the help of few-cycle pulses rather than multicycle millijoule-level pulses (see Appendixes). At lower intensities, the harmonic cutoff extends in agreement with the linear classical cutoff law of the three-step model (shown with a black line in Fig. 3) up to 38 eV at 32 TW cm^{-2}. Between 32 and 53 TW cm^{-2} the harmonic cutoff deviates from the linear cutoff law. Above 53 TW cm^{-2} the harmonic brightness is dramatically reduced, and the harmonics themselves distort significantly (see Appendixes). This can be explained by the generation of a plasma mirror at the front surface of the jet [21] [Fig. 1(b)]. However, we see that prior to the onset of the plasma mirror formation at 53 TW cm^{-2}, there remains a deviation from the linear cutoff law, above 32 TW cm^{-2}. This will be discussed further below.

Finally, by further compressing the pulse to 10.8 fs, i.e., 1.8 cycles, and selecting the intensity just below the threshold for creating a plasma, we optimize conditions to produce the highest-energy photons. Presented in Fig. 4 are harmonic spectra in this optimal condition, now reaching up to 50 eV, the highest reported in the condensed phase. We varied the CEP of this few-cycle pulse, and the influence of the change in CEP is clearly visible across the whole spectrum. The dependence is similar to a gas phase CEP scan, with half-cycle contributions appearing at the cutoff [31]. The observed CEP dependence further confirms, in conjunction with a spatially encoded arrangement for spectral phase interferometry for direct electric field reconstruction (SEA-SPIDER) measurement [32], that the driving pulse is an optimally compressed few-cycle pulse. The ellipticity dependence of the HHG is shown in the Appendixes and exhibits a smooth Gaussian dependence, measured below 53 TW cm^{-2}, similar to that observed in gas phase HHG.

We have demonstrated that higher-energy cutoffs, of the order of 45–50 eV, in liquid HHG are possible, provided that
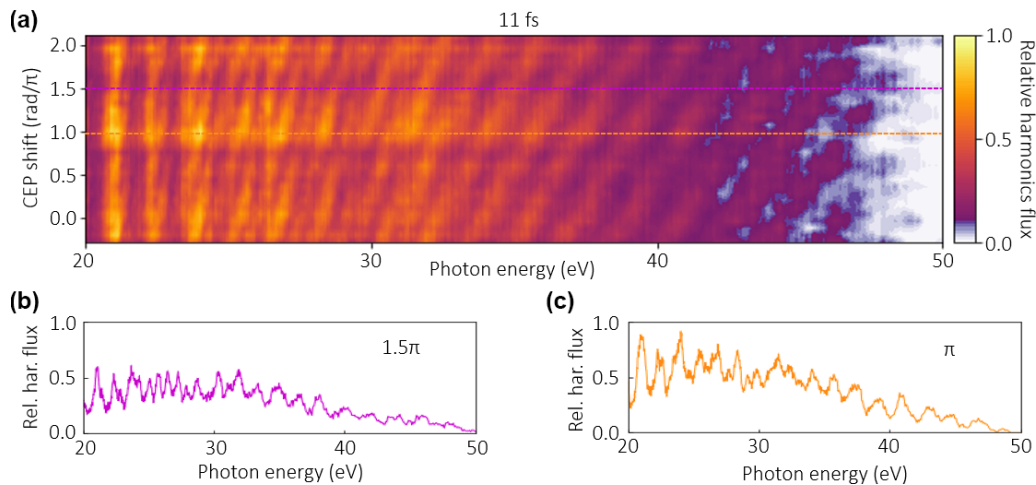
FIG. 4. (a) Dependence of the HHG spectrum of isopropanol, with 1.8-cycle, 10.8-fs pulses, on the CEP shift induced by a pair of fused silica wedges. The CEP is shifted by more than 2π rad, and a π periodicity is observed. Absolute CEP is unknown, and so zero CEP is set to coincide with maximum flux. (b) and (c) show line-outs at the horizontal dashed lines in (a) in their corresponding colors. Rel. har., relative harmonics.

the laser intensity is below the ionization saturation threshold, and this is aided by using an optimally compressed few-cycle pulse [33] and a longer-wavelength driver. Ultimately, the cutoff which can be achieved at one wavelength is limited by the intensity which can be reached before ionization saturation. This plays a similar role to that of laser damage in solids and over-the-barrier ionization in gases, which limits the intensity, and therefore the maximum possible cutoff energy. Higher intensities can be reached in liquids than in solids, as laser damage generally occurs before ionization saturation, and the highest intensities are reached in gases, which require intensities in excess of 120 TW cm^{-2}, even for an ionization potential of 10 eV. Although only a broad comparison, as the underlying physics of the three media are different, this is reflected in the highest observed HHG cutoffs observed in each.

The shortest possible pulse (1.8 cycles) produces the highest cutoff [34]. We achieve this result through specific experimental improvements: by calibrating the vapor pressure across the jet and choosing to work in a low-vapor regime; through careful calibration of the driving-field intensity transmitted through the jet, and therefore of the intensity at which plasma reflection occurs; and, finally, through verification of the pulse duration via a SEA-SPIDER and CEP stabilization. Our results appear to be consistent with a recombination picture of HHG, similar to the gas phase, with the additional feature of a deviation in the linear cutoff scaling occurring between 32 and 53 TW cm^{-2}. Above 53 TW cm^{-2}, ionization saturation occurs, and the cutoff energy reduces (see Fig. 3). As demonstrated for gas phase harmonics the observation of the CEP-dependent cutoff is a precursor to isolated attosecond pulse generation.

IV. SIMULATIONS

A. Modeling a dense medium, including propagation

We model the emission using a real-space recombination model to gain additional physical insight into electron scattering. However, in a thick medium a single-atom or single-molecule approach is not appropriate, and we therefore perform a full calculation which includes the linear and nonlinear propagation effects through the liquid. We simulate the harmonic spectra based on the strong-field approximation (SFA) [35] using a code that includes both an SFA kernel and full three-dimensional (3D) field propagation, benchmarked against gas-phase HHG measurements [36]. This full propagation calculation includes the effect of plasma dispersion on phase matching and the effect of defocusing on the driving-field intensity, although not explicitly the plasma mirror effect.

First, the jet is modeled as optically flat with a thickness of 2 μm in accordance with interferometrically measured values [13], and isopropanol is treated as a dense gas, but with an abrupt decay from liquid pressure to vapor pressure. We set the density to be consistent with the number density of isopropanol at 273 K (12 723 mol m^{-3}) For initial conditions, a transform-limited spatiotemporally Gaussian pulse was used with parameters matching the measured pulses. To compare these modeling results with the intensity-dependent data in Fig. 3, with cutoffs up to 45 eV, a 2.2-cycle pulse with a $1/e^2$ beam diameter of 260 μm is used. The laser propagates using the forward Maxwell equation in three dimensions with cylindrical symmetry (dispersion, paraxial diffraction, third-order nonlinearity, plasma dephasing, and absorption included). Instantaneous ionization rates are calculated using the Ammosov-Delone-Krainov (ADK) formula [37], and integration is performed using a preconditioned Runge-Kutta method with adaptive step sizing. Dispersion and diffraction are applied in the frequency domain, while nonlinear effects are applied in the real-space domain (split-step method). A standard hydrogen wave function with isopropanol's ionization potential is used, as a full treatment of molecules as emitters and electron-scattering targets is too complex to permit calculations along the full propagation that are needed to allow quantitative comparison with the measured spectra. This gives the expected spectrum for a dense medium without scattering.

B. Incorporation of scattering

In the application of a recombination model to the gas phase the role of the surrounding environment is typically not included. However, in the case of a dense medium, not only must propagation effects be included, but also the interaction of the electron trajectory with the neighboring molecules must be incorporated. To gain insight into the role of scattering from neighboring molecules, we develop further the recombination model: The electron wave packet following tunneling is considered free of the parent molecule, propagating and returning through the surrounding liquid, but now with finite probability of scattering off neighboring molecules. For both elastic and inelastic scattering, we consider a scattered electron as not contributing to the harmonic emission. Both types of scattering cause a spreading of the electron wave packet which reduces the recombination probability to a negligible amount and a phase shift (with an energy change for inelastic scattering) which precludes phase matching. This method can be seen as a logical extension of the strong-field approximation, for which the rescattering contribution from the parent nucleus is not included [38]. To include the influence of electron scattering, we apply an energy-dependent filter function which corresponds to a probability, for each kinetic energy of an electron, that the electron will have returned to its parent molecule without scattering.

For harmonic generation, the simulated laser field is resampled to a 1-μm spatial grid, and the single-atom HHG dipole is computed at every point using the strong-field approximation with stationary phase approximations used for the momentum and birth time integrals. The energy-dependent filter is applied to the harmonics before they are propagated to the end of the target region. Because the scattering probability increases substantially with trajectory time, long trajectories are expected to contribute minimally to the macroscopic harmonics. As such, temporal apodization is used to remove the contribution of the long trajectories and reduce computation time. The macroscopic field is then obtained by spatially integrating the HHG single-atom dipoles, accounting for paraxial diffraction, the local medium density, absorption, and dispersion as in the case without scattering.

C. Scattering probability calculation

The probability that an electron is not scattered along its trajectory is approximately the product of probabilities that the electron is not scattered for small time steps Δt between its birth and recombination.

$$p_{\text{n.s.}} = \prod_{i=1}^{N} 1 - p_i \Delta t, \qquad (1)$$

$$p_i = p_{\text{scat}}(t_0 + i\Delta t) \qquad (2)$$

$$N = \frac{t_{\text{rec}} - t_0}{\Delta t} \qquad (3)$$

where $p_{\text{scat}}(t)$ is the probability of scattering per unit time, at time t; and t_0 and t_{rec} are the birth and recombination times of the electron trajectory, respectively. Taking the natural

logarithm of both sides,

$$\ln p_{\text{n.s.}} = \sum_{i=1}^{N} \ln (1 - p_i \Delta t) \qquad (4)$$

$$= \sum_{i=1}^{N} \sum_{j=1}^{\infty} -\frac{1}{j} (p_i \Delta t)^j \qquad (5)$$

$$\approx -\sum_{i=1}^{N} p_i \Delta t, \qquad (6)$$

which becomes exact in the limit of number of steps N approaching infinity such that $\Delta t \to dt$.

$$\langle n \rangle = \sum_{j=1}^{N} p_j \Delta t \qquad (7)$$

is the average number of collisions that would occur for the electron following its classical, scattering-free trajectory. For infinite N,

$$\langle n \rangle = \int_{t_0}^{t_{\text{rec}}} p_{\text{scat}}(t) dt, \qquad (8)$$

$$p_{\text{n.s.}} = e^{-\langle n \rangle}. \qquad (9)$$

The problem is therefore reduced to determining and integrating the probability of the electron scattering per unit time. In this classical model, the probability of scattering is given by the probability of encountering a molecule along its path. Considering an infinitesimal time step,

$$p_{\text{scat}}(t) dt = \rho_N A(t) v(t) dt, \qquad (10)$$

where ρ_N is the number density of the molecules and $A(t)$ is their cross-sectional area. The time dependence of A accounts for the changing cross section with electron kinetic energy, which we include in our calculation. For low-energy electron-scattering cross sections, only vapor phase data currently exist, and we employ empirical values measured using a monochromatic electron beam in vapor phase isopropanol molecules [39] (see Appendixes). We assume that the cross section retains the same dependence on the electron kinetic energy but introduce a scaling factor, k, to vary the magnitude of the empirical cross-sectional data [39].

$$A(t) = \sigma'(t) = k\sigma_{\text{emp}}(t); \qquad (11)$$

$k = 1$ is equivalent to using a vapor cross-sectional area, i.e., a strong scattering contribution, and $k = 0$ when no scattering is included. We then have

$$p_{\text{n.s.}} = e^{-\int_{t_0}^{t_{\text{rec}}} p_{\text{scat}}(t) dt} \qquad (12)$$

$$= e^{-\int_{t_0}^{t_{\text{rec}}} \rho_N A(t) v(t) dt} \qquad (13)$$

$$= e^{-\int_{t_0}^{t_{\text{rec}}} \rho_N k\sigma_{emp.}(t) v(t) dt} \qquad (14)$$

This k factor is adopted because we do not expect monochromatic measurements in vapor phase isopropanol to accurately reflect the full dynamics of electron behavior in the liquid phase [40]. The data from these vapor phase measurements have been shown theoretically [22,23], experimentally [24,41], and in strong-field experiments [42] to overestimate the cross section in the condensed phase where correlation
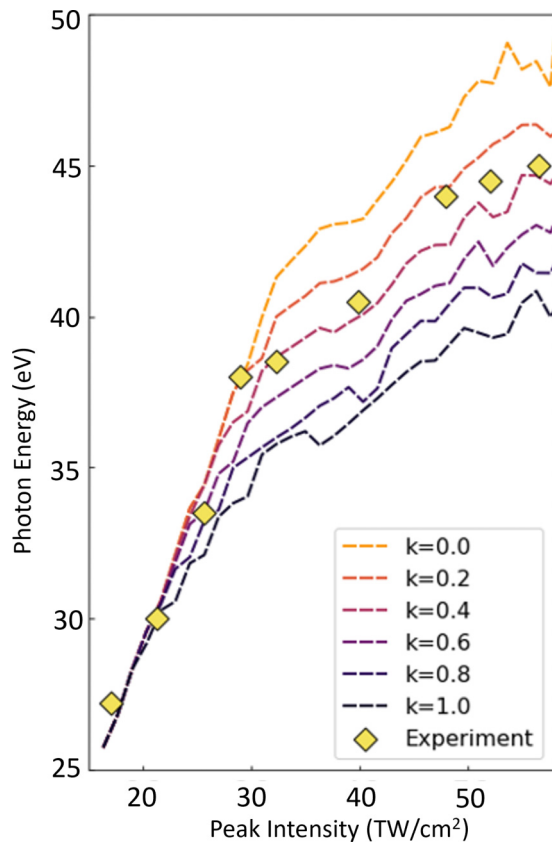
FIG. 5. A comparison between our experimental and simulation results of the dependence of the cutoff energy on laser-field peak intensity for a 13-fs driving pulse (2.2 cycles). The theoretical data are shown for varying values of k.

effects and charge screening events are present. Hence this approach allows us to explore the effect of electron scattering on liquid HHG emission by encompassing the screening and correlation of the higher-density medium into the single factor, k. By varying its magnitude, between 0 and 1, we can observe the impact of the kinetic-energy-dependent electron-scattering filter on the emission spectrum. When $k = 0$, we return to the dense medium calculation without scattering included. When $k = 1$, we include the empirical electron-scattering cross sections for vapor phase isopropanol. From the simulated intensity-dependent spectra (see Appendixes) and from the experimental data shown in Fig. 3, we extract the intensity dependence of the harmonic cutoff, and these results are shown in Fig. 5. We can see that the $k = 0$ (yellow line, no scattering) case broadly follows a linear cutoff law up to 32 TW cm^{-2}, after which ionization leads to phase shifts and defocusing. For $k = 1$, incorporating empirical electron-scattering values, we observe a growing deviation from the former case starting gradually at 24 TW cm^{-2} (29 eV) and resulting in a 10-eV difference in the cutoff at 50 TW cm^{-2}. When we compare the experimentally determined cutoffs (yellow diamonds), it is clear that these do not match the zero-scattering case ($k = 0$) or the case using empirical scattering values ($k = 1$). Some weak electron scattering is present to damp harmonic generation, below the breakdown threshold. We find that a value for k in the range from 0.2 to 0.4

provides a robust match to the experimental data, i.e., that the low-energy scattering cross section in isopropanol can be approximately a third less than that of the vapor phase measurements, due to electron screening in the liquid.

V. CONCLUSION

The evidence presented here, on high-harmonic generation in liquid isopropanol, when using few-cycle pulses below the liquid damage threshold, provides support for using a configuration-space recollision model to explore the HHG process in liquids. Through a simple but effective adaptation to SFA methods widely used in the gas phase, we can gain insight into the scattering of low-energy electrons in the liquid phase. Electron scattering reduces the number of coherent emitters. One of the implications is that, despite the potentially high density of emitters compared with that in gas, the harmonics emission is weakened. Unless this can be effectively compensated for, this limits the application of liquid HHG as a high-efficiency EUV source. However, as with HHG in the solid phase, HHG spectroscopy in liquids has the potential to probe the dynamics of scattering and spatial structure in the liquid environment. We hope this motivates the development of a more complete model that maps both the scattering amplitude and phase of the electron onto the final emission dipole. This could be applied to measuring low-energy electron scattering in liquids, which is important in radiation therapies [43,44]. Better determination of low-energy electron-scattering cross sections would contribute to more accurate modeling of electron damage mechanisms in tissue, for example, to understand better how DNA double bonds are damaged from low-energy electrons [45,46].

The data are held at Imperial College London and are available upon reasonable request to the corresponding author.

APPENDIX A: ULTRATHIN LIQUID JET TECHNOLOGY FOR IN-VACUUM USE

The target used for the experiments in this paper was a thin and flat sheet jet produced by the fan-spray nozzle presented by Galinis *et al.* [13]. This nozzle design ensures that the collision of jets necessary to create a thin sheet occurs within the interior of the nozzle preventing splashes and additional vapor generation. This is in contrast with systems where the collision occurs between two cylindrical jets in a vacuum.

During these experiments, isopropanol was run through the nozzle, backed by 1–5 bars of compressed nitrogen. For a new nozzle, 3 bars of pressure creates a sheet that is around 10 mm long and 1 mm wide at the middle, and 1–2 μm thick over the majority of its length. The velocity of the sheet under these conditions is 18.7 m s^{-1}, which ensures that between each shot at 1-kHz repetition rate the jet has moved 1.87 cm ensuring a totally fresh target for each shot. The spent liquid is captured by a collector. The entire liquid jet assembly is mounted in a vacuum chamber and is enclosed by a liquid-nitrogen-filled cold trap which keeps the vacuum below 10^{-3} mbar while the jet is running. Differential pumping separates the interaction chamber and the detection chamber (which is kept below 10^{-6} mbar). The large cold trap surrounding the jet has window-free ports for the laser and a side-view port for imaging and alignment of the jet. The sheet of liquid can run for up to 3 h before the enclosed cold trap is saturated with condensed isopropanol and the pressure rises too high for measurements.

APPENDIX B: VALIDATION OF THE LOW-VAPOR REGIME

1. Measurement of evaporative cooling of the jet

The liquid jet enters into a vacuum of below 10^{-3} mbar at a temperature of 20 °C. This generates a surrounding vapor layer through evaporation and a subsequent cooling due to the heat extraction for the phase change [47]. The evaporation-driven cooling creates a temperature and pressure gradient vertically along the jet. The temperature and vapor pressure are calculated in the following manner: The number of molecules N vaporizing from a surface A during a time interval δt is given by [48,49]

$$\frac{\delta N}{\delta t} = \frac{1}{\sqrt{2\pi m k_b T}} \times (p_{\text{vap}} - p)A, \tag{B1}$$

where m is the mass of one molecule, p_{vap} denotes the temperature-dependent vapor pressure, p is the pressure of the gas phase surrounding the jet, and T is the temperature of the liquid. The phase transition requires a negative evaporation enthalpy H_{vap} to be added to the liquid substance, leading to the temperature δT.

$$\delta T = \frac{H_{\text{vap}}}{N_A C M} \delta N, \tag{B2}$$

where N_A denotes the Avogadro constant, C denotes the specific heat, and M denotes the mass of the remaining liquid in the volume under consideration. Thus the cooling rate of the liquid jet can be estimated. The evaporation enthalpy H_{vap} is assumed to be constant over the temperature range of interest. This calculation was checked against measured data (see Table I and Ref. [14]), and good agreement was found. The liquid-vapor system here is modeled in the Knudsen diffusion regime, in which the evaporated molecules are propagating away from the source on ballistic, collision-free, trajectories [47], and the pressure drops as $1/r$. A correction is made to account for the jet molecules held back due to increased collisions at the surface, and a thicker vapor layer surrounds the initial surface jet before the Knudsen regime is reached.

TABLE I. In-vacuum measurement of the liquid jet temperature at different distances from the nozzle, recorded with a thermocouple probe.

Distance from nozzle (mm)	Temperature (°C)
1	10.6
3.5	−5.5
5	−9.5
7.5	−19.5
10	−20

2. Isopropanol absorption length in the EUV region

The harmonics generated in the liquid will travel through the isopropanol vapor residing at the rear surface of the jet. The absorption length depends on the vapor pressure, and therefore the height of the input pulse on the jet (Fig. 6). At the top of the jet (Pos1), the absorption length is a few hundreds of micrometers so the absorption peak at 15 eV can be clearly seen on the harmonics spectrum. As the absorption length is increasing from the top to the bottom of the jet, the harmonics are less absorbed. The isopropanol vapor densities are calculated from ideal gas law with temperatures and pressures of the surrounding vapor. The absorption length of liquid isopropanol is a few tens of nanometers. The absorption lengths are calculated from available experimental absorption cross sections [29].

3. Vapor plume at high intensity

When the laser intensity is above the ionization saturation threshold, a bright vapor plume appears on the front surface of the jet, as seen in Fig. 7. The appearance of this plume is useful for locating the interaction point on the surface of the jet.
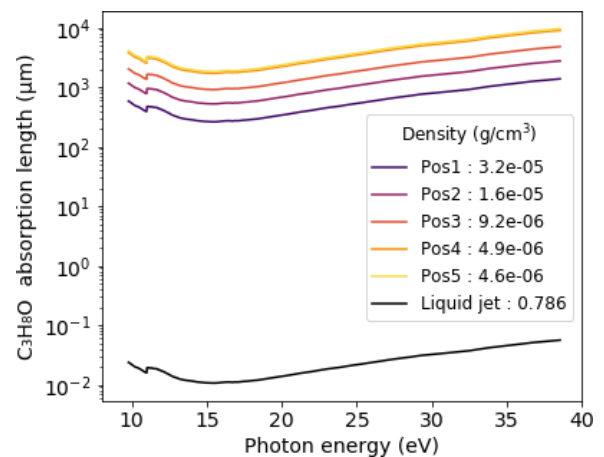

FIG. 6. Absorption length of isopropanol at different densities in the EUV region, representative of vapor densities at five different positions from the top (Pos1) to the bottom of the jet (Pos5). Here, 3.2e-05, 3.2×10^{-5}.
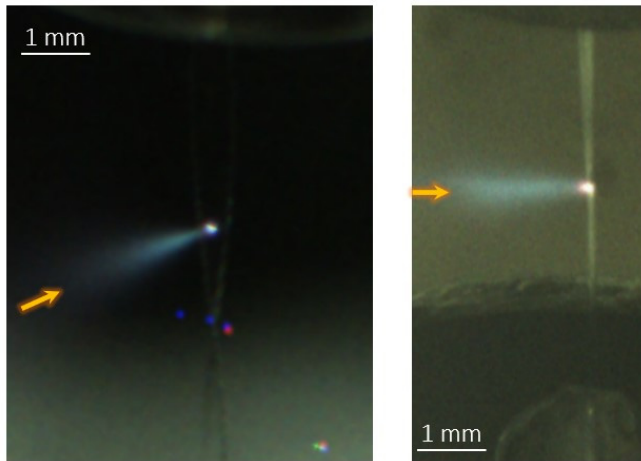
FIG. 7. Pictures of the vapor plume appearing on the front surface of the liquid jet at laser peak intensities exceeding the breakdown threshold. No plume is observed below this threshold. The laser direction is indicated by an orange arrow.

4. Parallel scan

One of the tests we perform of the vapor contribution to the observed harmonics is measurement of harmonics with the laser parallel to the jet surface, as in Fig. 2(c) of the main text. It is important to consider the proximity of the laser focus to the jet surface and how representative the vapor density is of the density observed in normal incidence. The density near a liquid surface is analogous to electric field near a charge or charged surface, as the flux of molecules is formally equivalent to Gauss's law. The pressure near a point source therefore follows an inverse square law. Also analogous to electrodynamics, the pressure near a surface is approximately constant, over a length characterized by the dimensions of the surface, i.e., the width and length of the surface. In our case, this is significantly much more than an order of magnitude larger than the beam waist. We have calculated the vapor density near a liquid sheet, using the same approach as we discuss in Ref. [25]. By integrating over the lateral axis, the areal density of the beam moving away from the surface of the jet is found to reduce by only a factor of 3 over 400 µm, significantly more than the beam waist. Figure 8 shows the harmonic spectrum measured at high intensity, which is necessary to measure any signal in our setup. At the lower intensities of the main text, no harmonic emission is observed.

5. Excess pressure from laser heating

There are two additional processes which could arise from laser-induced evaporation from the jet and so could potentially lead to additional density of vapor in the vicinity of the focal region, and we therefore address this issue here. Under the conditions of our experiment, i.e., below the ionization threshold, the jet remains transparent, and very little laser energy is deposited in the liquid [21]. Absorption excluding plasma is approximately 0.7% in 2 µm of isopropanol [50]. All the absorption due to plasma occurs on the front side of the jet with a depth usually considered to be 10% of the laser wavelength, i.e., 180 nm in our case. The heating is a "slow"
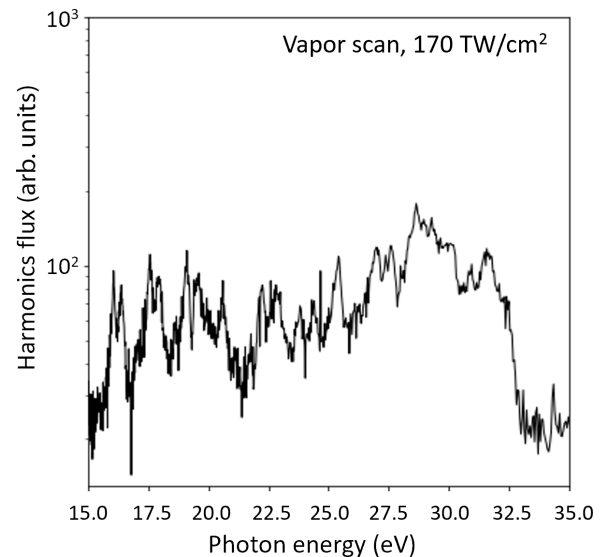

FIG. 8. Harmonics spectrum at a peak intensity of 170 TW cm^{-2} when the laser beam is parallel and close to the liquid jet [see Fig. 2(c) of the main text]. At 50 TW cm^{-2}, no signal is observed in this configuration.

process (greater than picoseconds); so the jet sees no heating during the laser interaction, and the next shot sees a fresh surface. Even so, we consider two additional effects which may cause additional pressure surrounding the jet at the interaction region. The first is a buildup of pressure at the position of the jet due to heating. The second is the gradual heating of the jet due to heat dissipation. Taking a conservative estimate of a 100-µm beam waist and 200-µJ pulse, the illuminated volume is heated by only 33 K. During the thermalization, the heat will diffuse into the rest of the sample and into vapor. First, we consider the accumulated heat in the jet due to dissipation (without dissipation the heat never "reaches" the next interaction volume of the jet). The rate at which the illuminated spot cools can be calculated from the heat equation, which because we are in the nonsaturating regime we can reduce to the cylindrically symmetric case of heat spreading only radially from the beam center: This does not include cooling at the surfaces; so will overestimate the heating effect. We solve the heat equation for temperature $u(x, t)$

$$\frac{du}{dt}(x, t) = D\nabla^2 u(x, t), \tag{B3}$$

$$D = \frac{k}{c_p \rho}, \tag{B4}$$

where ρ is the density, k is the thermal conductivity, and c_p is the specific heat capacity. For the initial value problem of a radius of 100 µm initially heated to 303 K and everywhere else at 270 K, we propagate using the Crank-Nicolson method, the result of which is shown in Fig. 9. During the time between laser shots (1 ms), negligible heat is transferred between the position of the previous focus on the jet and the next focus (approximately 20 mm away). We can therefore rule out the gradual heating of the jet. Next, we consider the buildup of pressure due to evaporation from the laser-heated area in previous shots. Given that the thermal energy remains localized
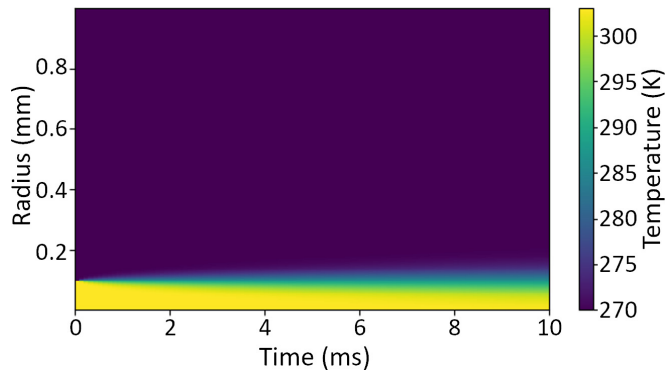
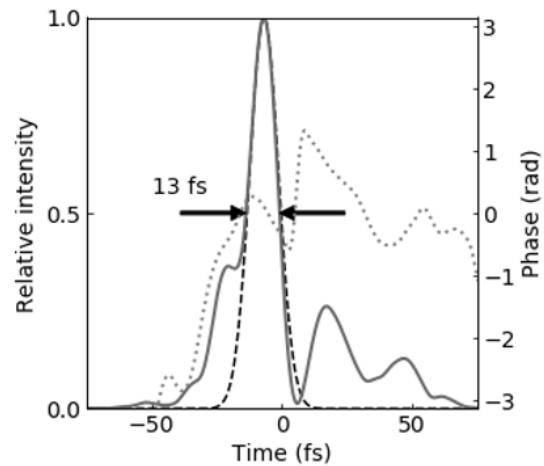FIG. 9. Calculated heat diffusion of an irradiated liquid target.

FIG. 10. A temporal profile of the pulses measured with a scanning SHG-FROG. The pulses exhibit a duration of 13 fs at FWHM. The Gaussian fit of the main peak is shown with the dashed line.

to the position of the previous jet and is moving at approximately 20 m s^{-1}, for an approximate focal spot diameter of 200 µm, the heated area is only evacuating into the vicinity of the jet 1% of the time. The characteristic velocity of the diffusion can be taken to be the diffusion coefficient divided by a characteristic length scale, for which the 200 µm is the most logical choice. The diffusion coefficient for isopropanol vapor in isopropanol vapor is not available in the literature, but values between 0.1 and 1 cm^2 s^{-1} are typical [51] at atmospheric pressure. Taking the lower end of this range, and adjusting to 10 mbar, the characteristic velocity is 5 m s^{-1}. It is clear to see, therefore, that the very small surface of the jet, dissipating at a rate of 5 m s^{-1} into a 3D volume and anyway localized for only 1% of the duty cycle, will have a negligible effect on the pressure local to the interaction region. We know that the global pressure is unchanged, because this is measured during the experiment. Using the best data available to quantify the gas vapor pressure—even close to the surface of the jet—the density length product is an order of magnitude lower than that required to generate vapor phase harmonics in typical organic molecules with similar ionization potential [52].

APPENDIX C: MEASUREMENT AND CALIBRATION OF LASER PARAMETERS

1. Laser system

The laser pulses were generated from a high-energy optical parametric amplifier (HE-TOPAS, Light Conversion, 40 fs, 1.8 µm, 1.2 mJ) pumped by a commercial, but extensively customized, 1-kHz Ti:sapphire amplifier (Red Dragon, KMLabs and Crunch Technologies, 30 fs, 800 nm, 8 mJ). The idler pulses were compressed to between 11 and 15 fs, which corresponds to approximately two optical cycles, using an argon-filled hollow-core fiber followed by a fused silica wedge-pair compressor. Compressed pulses of 0.5 mJ are available at 1.8 µm. The laser pulses were delivered to the interaction region by a 50-cm focal length lens. The jet assembly was mounted on three-axis manipulator arms, which allowed us to translate the jet with respect to the laser beam. An iris, situated before the lens, was used to clip the outer regions of the beam profile and therefore to vary the peak intensity of the driving field in the interaction region. The pulse energy was measured after the iris and before the lens. The ellipticity was varied using a quarter-wave plate. The

CEP was controlled by translating one of the fused silica compressor wedges with respect to the other. The full scan shown in Fig. 4 of the main text represents an insertion of ∼100 µm of fused silica and lasted approximately 1.5 h. Due to the low dispersion but large difference between group velocity and phase velocity at 1.8 µm and the deployment of a few-cycle pulse, no significant changes in pulse compression are caused by the wedge scan, and thus no envelope effects are observed, which are otherwise common at 0.8 µm [53].

2. Pulse transmission measurements

The driving 1800-nm pulse was focused into the liquid jet sheet, and the focal plane was imaged onto a charge-coupled device (CCD) camera which measured the spatial profile. This also allowed the change in transmission with respect to increasing peak intensity to be mapped. This is shown in Fig. 1(b) of the main text with further details in Ref. [17].

3. Pulse duration measurement

We measured the temporal profile of our pulses using a homemade scanning second-harmonic-generation frequency-resolved optical gating (SHG-FROG) device (see Fig. 10) and with a spatially encoded arrangement for filter-based spectral phase interferometry for direct electric field reconstruction (SEA-F-SPIDER) [36] (see Fig. 11). The SEA-F-SPIDER has a better isolated signal than a SHG-FROG device when measuring pulses with sufficient bandwidth that the second and third harmonic begin to overlap, and allows for direct phase retrieval. We calculate the peak intensity using the energy contained in the central spike, not the pedestal.

4. Laser intensity calibration

The peak intensity was calculated using standard formulas for focusing of Gaussian beams, with corrections for reflection losses in the uncoated calcium fluoride lens and the uncoated fused silica window at 1.8 µm, and from the liquid surface itself, as well as corrections to the focus radius
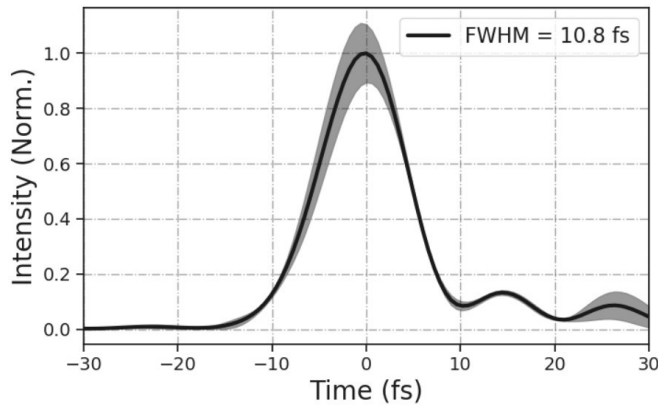
FIG. 11. The temporal profile of the shortest pulses measured with a SEA-SPIDER. The pulses exhibit a duration of 10.8 fs at FWHM. Norm., normalized.
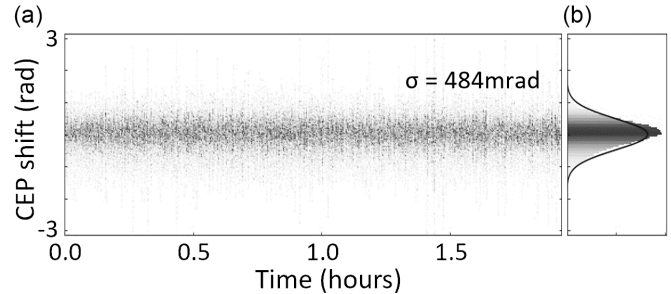

FIG. 12. Carrier envelope phase stability. (a) Probability density function (PDF) of the CEP as a function of time, acquired during the scan presented in Fig. 4 of the main text. The CEP stability is measured with 10 ms integration time (ten pulses). Only one of every eight data points is recorded. (b) PDF of the CEP shift over the entire scan. The Gaussian fit is shown in black. The standard deviation is 484 mrad.

when apodizing a beam with an iris (Fourier optics). In the case of a few-cycle pulse, we calculate the peak intensity based on the energy contained in the central spike, not the pedestals.

$$I_{\text{peak}}(w_g) = 0.94 \frac{2E_p}{\tau_p \pi w_g^2}, \tag{C1}$$

$$w_g = 2\sqrt{(w_0)^2 + (0.45 \times \lambda \times 500/D)^2}, \tag{C2}$$

$$w_0 = \frac{f\lambda}{w_r \pi}, \tag{C3}$$

where f is the focal length (500 mm), w_r is the waist at the lens entrance, w_g is the corrected focus radius validated using the transmitted beam measurements, D is the iris diameter, E_p is the pulse energy measured after the iris and corrected to take into account the losses, and τ_p is the pulse duration at full width at half maximum (FWHM).

In our setup, for example, if the iris is closed to a diameter of 10.5 mm, the measured pulse energy is 200 µJ, and the corrected focus radius is 113 µm. With these parameters and this loss correction, a pulse duration of 13 fs leads to a peak intensity of approximately 50 TW cm^{-2}.

Finally, our intensity calculations were further cross-checked against the CEP-dependent spectral cutoff energies observed when the liquid jet is replaced with a krypton gas target. The intensity dependence has been shown to be accurately described by the classical cutoff law within 3% at this wavelength [54], with little impact of phase-matching conditions. This is consistent with other values observed in the literature [55]. We note that the saturation intensity for krypton is 247 TW cm^{-2} at 1800 nm for a 12-fs pulse duration [54]. We were also able to quantify the beam radius by reimaging the focus onto a camera. Intensity measurements are frequently overestimated due to beam imperfections, and we estimate a typical error range of ± 5 TW cm^{-2}, from shifts in pedestal-pulse heights, error on the iris diameter measurement, and error on the beam waist. Cutoff measurements were taken where EUV light falls below the microchannel plate (MCP) noise floor, with an estimated error of ± 2.5 eV.

5. Carrier envelope phase stability

Although passive carrier envelope phase (CEP) stability is provided by the idler output of an optical parametric amplifier (OPA), slow drifts such as those due to air currents created the need for active stabilization. CEP stability was measured using the phase of spectral interference fringes between the second and third harmonic of the driving field (Fig. 12). The third harmonic was available in the experiment as a by-product of the spectral broadening in the gas-filled hollow core fiber, and the second harmonic was generated using a beta barium borate crystal. A piezoelectric mirror in the pump arm of the third amplification stage of the OPA was used to lock the delay and thereby phase drifts between the pump and seed, which in turn compensates for slow drifts of the CEP of the idler [36].

6. Calibration of CEP and intensity using krypton and relative flux

Our measurements of intensity and of CEP were susceptible to errors (manufacturing errors in the angle of our wedges, literature values for group and phase velocity, focal spot measurement, etc.). Therefore it was important to verify these from a direct measurement at the interaction region. For this reason we decided to perform measurements of the CEP dependence of a well-studied noble gas, krypton (Fig. 13). Krypton was chosen due to its low ionization
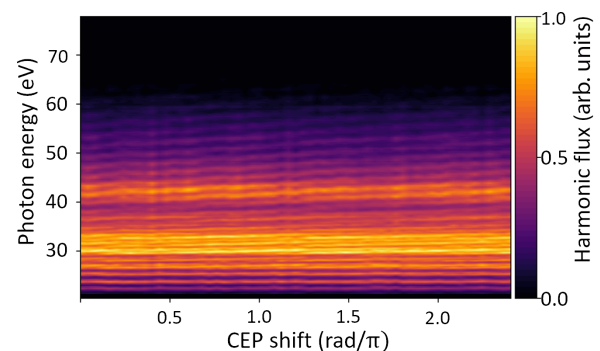

FIG. 13. Krypton CEP-dependent harmonics for calibration.

potential (14 eV), which is more comparable to isopropanol than, for instance, helium. To ensure the same interaction point, the krypton target was delivered through the same nozzle as the liquid isopropanol sheets. To achieve maximal flux, the interaction region was chosen to be as close to the nozzle as could be achieved.

These data allowed us to calibrate our wedge scans from the known CEP periodicity of noble gases. The extension of the cutoff harmonics also verifies that they were not clamped by ionization effects. This is further evidenced by the cutoff of approximately 62 eV, which is far below the expected cutoff if we were close to the intensity required for over-the-barrier ionization (142.5 eV for an 1800-nm driving field with a peak intensity of 134 TW cm^{-2}).

Although it is not possible to calibrate the total pulse energy or spectral power distribution with an MCP detector, and without a well-defined EUV source for comparison, it is possible to make a comparison between our krypton and liquid isopropanol measurements. Under the same conditions, we find that the spectral power density in krypton is approximately 20–50 times higher in the plateau region.

APPENDIX D: EUV DETECTION SYSTEM AND CALIBRATION

The spectrum was recorded using a home-built flat-field spectrometer consisting of an 250 μm slit, a 1200 lines/mm variable-line-spacing flat-field grating (Hitachi 001-0437), and a cesium-iodine-coated 40-mm-diameter microchannel plate (MCP) with a backside-mounted phosphor screen (Photonis). The fluorescence of the phosphor screen is collected using a PCO Pixelfly camera. The slit and grating were fully motorized in order to optimize the spectral resolution. The MCP and camera assembly is furthermore translatable along the diffraction direction in order to record the full harmonic spectrum. The spectrometer was calibrated using the approximately linear wavelength scaling at small angles of incidence and reflection together with metallic absorption edges in aluminium, zirconium, and tin in the relevant region, i.e., at 15, 25, 55, and 72 eV. Cutoff measurements were taken where EUV light falls below the MCP noise floor, with an estimated error of ±2.5 eV.

APPENDIX E: INTENSITY DEPENDENCE OF THE HARMONIC YIELD

The yield of each harmonic and its dependence on input intensity were for measured for a 1800-nm, 2.2-cycle pulse, incident on the liquid jet (i.e., MCP data shown in Fig. 3 of the main text). Figure 14 shows clearly the two separate damping processes which occur as the intensity is increased. First, the reduction of the harmonic yield for lower-energy harmonics is visible from 35 TW cm^{-2}, despite a still linearly increasing cutoff, i.e., new higher-energy harmonics continue to emerge. Second, at 50 TW cm^{-2} all harmonics are damped at a faster rate, giving a rapid reduction in all harmonic emission yields. The first process is attributed to electron scattering, while the second process can be correlated with the increased ionization, creation of a plasma mirror, and therefore decreasing input laser intensity within the jet.
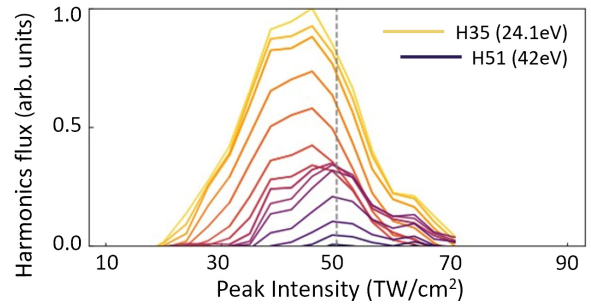

FIG. 14. Dependence of the harmonics flux on driving-field peak intensity, for harmonics 35–51 (H35–H51; Fig. 3 of the main text). A clear drop in the harmonics flux is observed above the breakdown threshold of the liquid.

APPENDIX F: NUMERICAL MODELING OF HHG IN ISOPROPANOL

Here we show numerical simulations of HHG spectra from our liquid target. Figure 15(a) shows calculated harmonic spectra as a function of the laser intensity with a full vapor phase scattering cross section ($k = 1$). This leads to significant
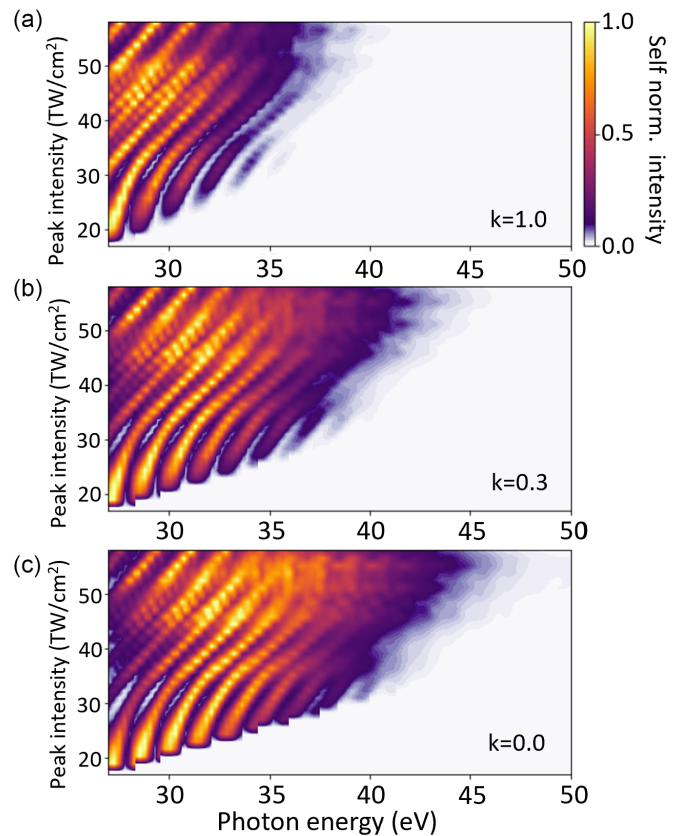
FIG. 15. Numerical modeling. Numerical modeling of high-harmonic generation in isopropanol-like dense media using a semiclassical strong-field approximation, corresponding to experimental conditions. (a) A scattering probability calculation is incorporated with $k = 1$ (see main text). The higher-energy trajectories are strongly damped through interactions with neighboring molecules. (b) $k = 0.3$. (c) $k = 0$, i.e., no scattering. The harmonic intensity is self-normalized.

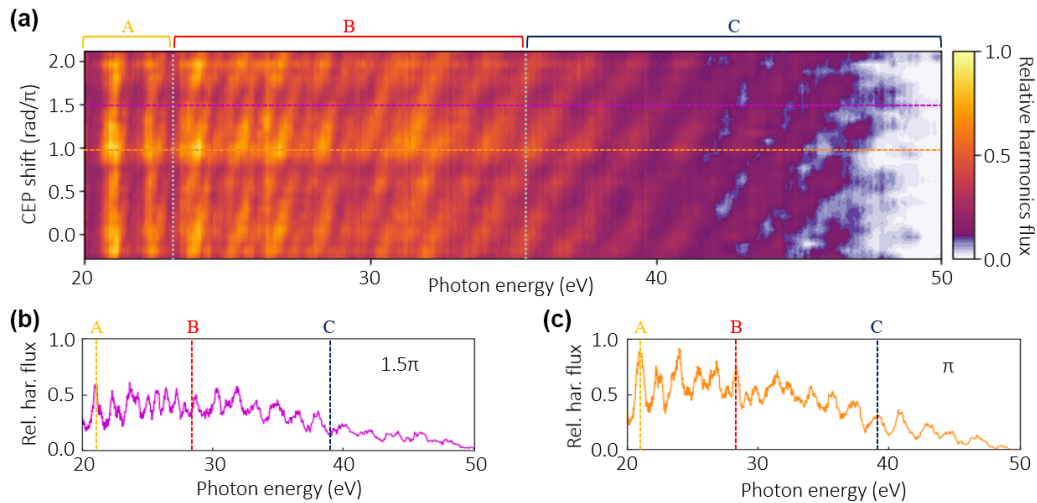FIG. 16. (a) Dependence of the harmonics from liquid on the CEP shift induced by a pair of fused silica wedges. As the absolute CEP is unknown, we set the zero CEP to coincide with a maximum flux. Three different regions (regions A, B, and C) are indicated. (b) and (c) Line-outs at the horizontal dashed lines in (a) are shown in their corresponding colors.

damping, which does not accurately model the experimental data. Figure 15(b) ($k = 0.3$) better matches the experimental data, with the highest-energy emission still present, but damp-ened to the point that the harmonic cutoff appears reduced. Figure 15(c) ($k = 0$) shows the unscattered calculation. When we compare the experimentally determined cutoffs with the cutoffs from the simulated data for various k, it is clear again that weak electron scattering is present to damp harmonic generation, below the breakdown threshold (53 TW cm^{-2}), but does not significantly reduce the cutoff. Note that the

modeling was performed for a pulse of 13 fs; so the modeling is in the same conditions as the intensity scan shown in Fig. 3 of the main text.

APPENDIX G: ADDITIONAL HIGH-HARMONIC MEASUREMENTS

1. CEP dependence of harmonics from liquid

Presented in Figs. 16(a)–16(c) are harmonic spectra from liquid reaching up to 50 eV, where the influence of the change
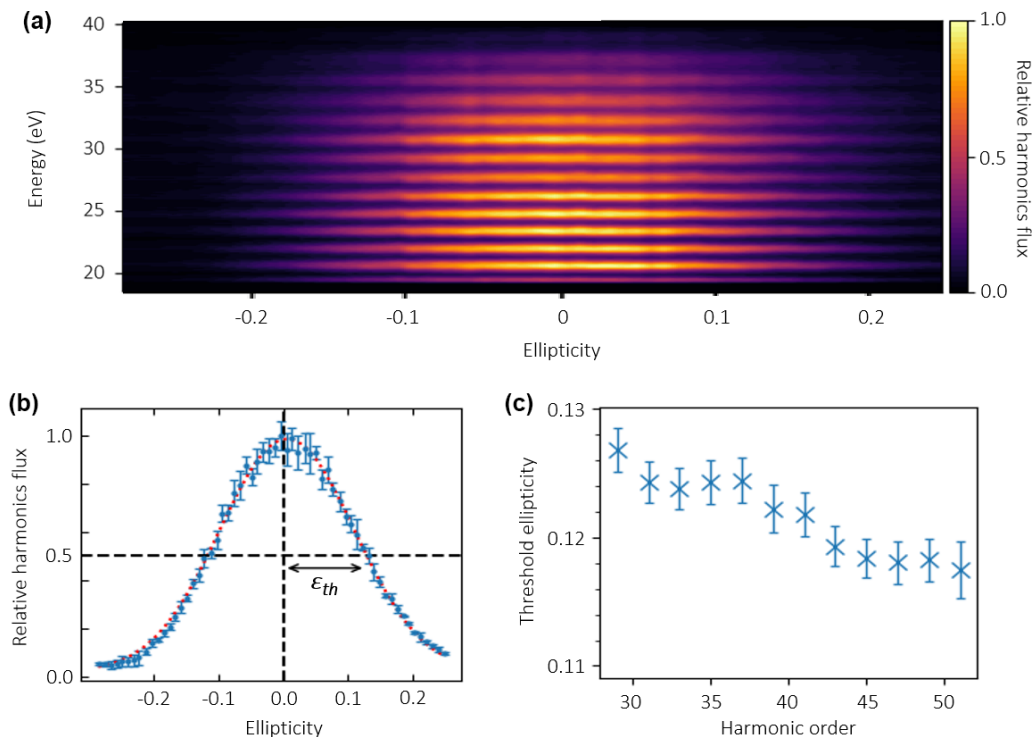

FIG. 17. Ellipticity measurements. (a) High-harmonic dependence on changing ellipticity. (b) Ellipticity of the 37th harmonic. (c) Ellip-ticity threshold for each harmonic. Error bars represent the standard deviation.
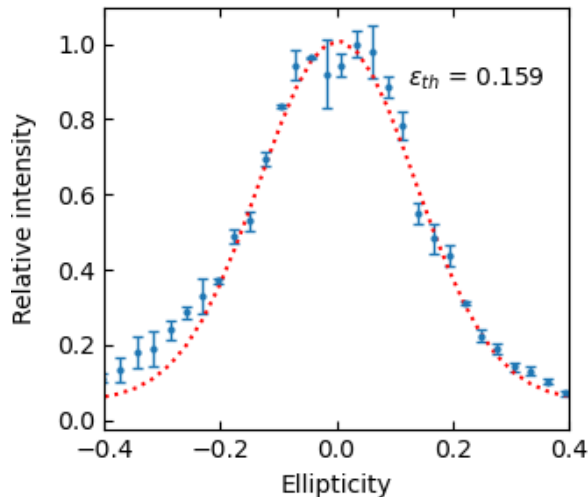
FIG. 18. Harmonic intensity vs ellipticity, above the breakdown threshold. Error bars represent the standard deviation. The Gaussian fit is shown with a red dotted line.

in the CEP across the whole HHG spectrum is clearly visible. The dependence is typical of gas phase harmonics [31] although this pattern has also been observed in interband HHG in MgO [56]. The high-energy region (region C) offers insight into the time structure of the harmonics. Half-cycle interference manifests as the well-known shift between even and odd harmonics as the number of contributing half cycles shifts between even and odd numbers. This is evidence that with a slightly shorter pulse, isolated attosecond pulses would be generated from the liquid. In region A the number

of contributing half cycles is so high that only the flux is varied as a function of CEP, while region B is an intermediate regime.

2. Ellipticity measurements

Utilizing pulses below the breakdown limit, we also performed measurements of the dependence of the high-harmonic generation on the ellipticity of the driving field. The ellipticity was rotated using a $\lambda/4$-wave plate. The rotation of the major axis of the ellipticity was not corrected as doing so would necessitate additional dispersive optics. In a separate set of measurements, utilizing linear polarization, there was no detectable effect on the high harmonics when rotating the major axis using a $\lambda/2$-wave plate. Figure 17 shows the result of changing the driving field's ellipticity. The harmonics generated in gases generally show a Gaussian dependence on the ellipticity of the driving field, peaking at zero ellipticity. This is typical of a recombination model for harmonic energies far above the ionization potential, where the ionized electrons enter the continuum with negligible transverse momentum. To quantify a difference in behavior between individual harmonics, we parametrize this Gaussian dependence using the ellipticity threshold at which the harmonic flux of a given harmonic is reduced to a half. This is determined from the half width at half maximum of a fit to the harmonic flux as a function of ellipticity, as demonstrated in Fig. 17(b). Figure 17(c) shows that, in general, the ellipticity threshold decreases with increasing harmonic order. This indicates that higher harmonic orders are more dependent on the ellipticity and is consistent with increased
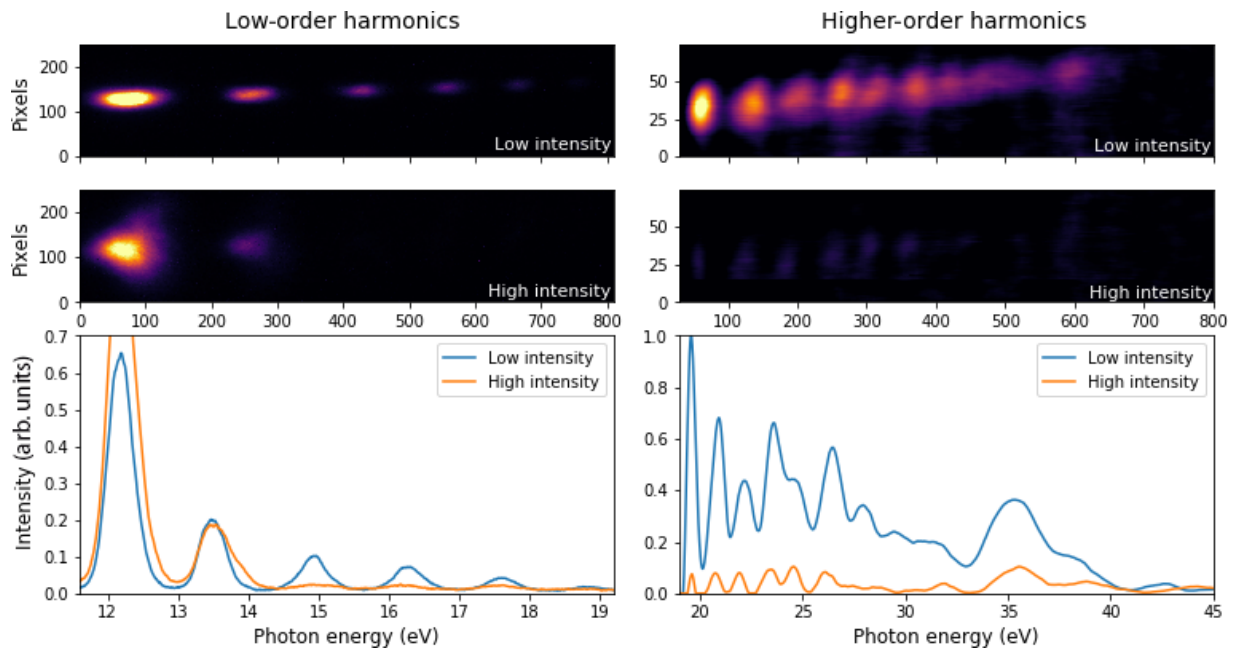
FIG. 19. Comparison between low- and high-intensity harmonics with a CEP-stable few-cycle idler beam (1800 nm) at two MCP positions. Low peak intensity, 48 TW cm^{-2}; high peak intensity, 70 TW cm^{-2}. Increasing the intensity above a certain threshold leads to a reshaping of the first harmonics, which can be due to a plasma lens, and drastically reduces the signal above 15 eV. Note that there is some space-energy mapping of the harmonics, which is the familiar "attosecond lighthouse" [57] caused by spatial chirp introduced by our wedge compressor. This was corrected for later measurements, as can be seen in the main text.

displacement of the electron wave packet upon recombination as is the case for short-trajectory harmonics. In an additional set of measurements, just above the breakdown threshold, we were able to identify broadening of the ellipticity dependence due to intensity clamping at linear polarization (see Fig. 18).

3. Comparison of harmonics above and below the breakdown threshold

Figure 19 shows a comparison of the HHG spectrum on either side of the breakdown threshold. Above the threshold a significant reshaping of the harmonics is observed, and the signal is drastically reduced above 15 eV.

[1] M. Hentschel, R. Kienberger, C. Spielmann, G. A. Reider, N. Milosevic, T. Brabec, P. Corkum, U. Heinzmann, M. Drescher, and F. Krausz, Attosecond metrology, Nature (London) **414**, 509 (2001).

[2] P. M. Paul, E. S. Toma, P. Breger, G. Mullot, F. Augé, P. Balcou, H. G. Muller, and P. Agostini, Observation of a train of attosecond pulses from high harmonic generation, Science **292**, 1689 (2001).

[3] S. Baker, J. S. Robinson, C. A. Haworth, H. Teng, R. A. Smith, C. C. Chirila, M. Lein, J. W. G. Tisch, and J. P. Marangos, Probing proton dynamics in molecules on an attosecond time scale, Science **312**, 424 (2006).

[4] M. Kotur, D. Guénot, Á. Jiménez-Galán, D. Kroon, E. W. Larsen, M. Louisy, S. Bengtsson, M. Miranda, J. Mauritsson, C. L. Arnold, S. E. Canton, M. Gisselbrecht, T. Carette, J. M. Dahlström, E. Lindroth, A. Maquet, L. Argenti, F. Martín, and A. L'Huillier, Spectral phase measurement of a Fano resonance using tunable attosecond pulses, Nat. Commun. **7**, 10566 (2016).

[5] Y. Pertot, C. Schmidt, M. Matthews, A. Chauvet, M. Huppert, V. Svoboda, A. von Conta, A. Tehlar, D. Baykusheva, J.-P. Wolf, and H. J. Wörner, Time-resolved x-ray absorption spectroscopy with a water window high-harmonic source, Science **355**, 264 (2017).

[6] S. Ghimire, A. D. DiChiara, E. Sistrunk, P. Agostini, L. F. DiMauro, and D. A. Reis, Observation of high-order harmonic generation in a bulk crystal, Nat. Phys. **7**, 138 (2011).

[7] Y. S. You, Y. Yin, Y. Wu, A. Chew, X. Ren, F. Zhuang, S. Gholam-Mirzaei, M. Chini, Z. Chang, and S. Ghimire, High-harmonic generation in amorphous solids, Nat. Commun. **8**, 724 (2017).

[8] S. Ghimire and D. A. Reis, High-harmonic generation from solids, Nat. Phys. **15**, 10 (2019).

[9] M. Garg, M. Zhan, T. T. Luu, H. Lakhotia, T. Klostermann, A. Guggenmos, and E. Goulielmakis, Multi-petahertz electronic metrology, Nature (London) **538**, 359 (2016).

[10] H. G. Kurz, D. S. Steingrube, D. Ristau, M. Lein, U. Morgner, and M. Kovačev, High-order-harmonic generation from dense water microdroplets, Phys. Rev. A **87**, 063811 (2013).

[11] A. D. DiChiara, E. Sistrunk, T. A. Miller, P. Agostini, and L. F. DiMauro, An investigation of harmonic generation in liquid media with a mid-infrared laser, Opt. Express **17**, 20959 (2009).

[12] T. T. Luu, Z. Yin, A. Jain, T. Gaumnitz, Y. Pertot, J. Ma, and H. J. Wörner, Extreme-ultraviolet high-harmonic generation in liquids, Nat. Commun. **9**, 3723 (2018).

[13] G. Galinis, J. Strucka, J. C. T. Barnard, A. Braun, R. A. Smith, and J. P. Marangos, Micrometer-thickness liquid sheet jets flowing in vacuum, Rev. Sci. Instrum. **88**, 083117 (2017).

[14] M. Ekimova, W. Quevedo, M. Faubel, P. Wernet, and E. T. J. Nibbering, A liquid flatjet system for solution phase soft-x-ray spectroscopy, Struct. Dyn. **2**, 054301 (2015).

[15] I. Crassee, L. Gallmann, G. Gäumann, M. Matthews, H. Yanagisawa, T. Feurer, M. Hengsberger, U. Keller, J. Osterwalder, H. J. Wörner, and J. P. Wolf, Strong field transient manipulation of electronic states and bands, Struct. Dyn. **4**, 061505 (2017).

[16] C.-M. Wang, N. Tancogne-Dejean, M. Altarelli, A. Rubio, and S. A. Sato, Role of electron scattering on the high-order harmonic generation from solids, Phys. Rev. Res. **2**, 033333 (2020).

[17] Y. S. You, E. Cunningham, D. A. Reis, and S. Ghimire, Probing periodic potential of crystals via strong-field re-scattering, J. Phys. B: At., Mol. Opt. Phys. **51**, 114002 (2018).

[18] M. M. S., A. Pattanayak, M. Ivanov, and G. Dixit, Direct numerical observation of real-space recollision in high-order harmonic generation from solids, Phys. Rev. A **100**, 043420 (2019).

[19] E. N. Osika, A. Chacón, L. Ortmann, N. Suárez, J. A. Pérez-Hernández, B. Szafran, M. F. Ciappina, F. Sols, A. S. Landsman, and M. Lewenstein, Wannier-Bloch approach to localization in high-harmonics generation in solids, Phys. Rev. X **7**, 021017 (2017).

[20] A. W. Zeng and X. B. Bian, Impact of statistical fluctuations on high harmonic generation in liquids, Phys. Rev. Lett. **124**, 203901 (2020).

[21] C. Ferchaud, S. Jarosch, T. Avni, O. Alexander, J. C. Barnard, W. Larsen, M. R. Matthews, and J. P. Marangos, Interaction of an intense few-cycle infrared laser pulse with an ultrathin transparent liquid sheet, Opt. Express **30**, 34684 (2022).

[22] N. Sinha and B. Antony, Mean free paths and cross sections for electron scattering from liquid water, J. Phys. Chem. B **125**, 5479 (2021).

[23] R. Signorell, Electron scattering in liquid water and amorphous ice: A striking resemblance, Phys. Rev. Lett. **124**, 205501 (2020).

[24] T. E. Gartmann, S. Hartweg, L. Ban, E. Chasovskikh, B. L. Yoder, and R. Signorell, Electron scattering in large water clusters from photoelectron imaging with high harmonic radiation, Phys. Chem. Chem. Phys. **20**, 16364 (2018).

[25] J. C. Barnard, J. P. Lee, O. Alexander, S. Jarosch, D. Garratt, R. Picciuto, K. Kowalczyk, C. Ferchaud, A. Gregory, M. Matthews, and J. P. Marangos, Delivery of stable ultra-thin liquid sheets in vacuum for biochemical spectroscopy, Front. Mol. Biosci. **9**, 1044610 (2022).

[26] I. Mirza, N. M. Bulgakova, J. Tomáštík, V. Michálek, O. Haderka, L. Fekete, and T. Mocek, Ultrashort pulse laser ablation of dielectrics: Thresholds, mechanisms, role of breakdown, Sci. Rep. **6**, 39133 (2016).

[27] P. Zhokhov and A. Zheltikov, Optical breakdown of solids by few-cycle laser pulses, Sci. Rep. **8**, 1824 (2018).

[28] J. D. Koralek, J. B. Kim, P. Brůža, C. B. Curry, Z. Chen, H. A. Bechtel, A. A. Cordones, P. Sperling, S. Toleikis, J. F. Kern,

S. P. Moeller, S. H. Glenzer, and D. P. DePonte, Generation and characterization of ultrathin free-flowing liquid sheets, Nat. Commun. **9**, 1353 (2018).

[29] H. Koizumi, K. Hironaka, K. Shinsaka, S. Arai, H. Nakazawa, A. Kimura, Y. Hatano, Y. Ito, Y. Zhang, A. Yagishita, K. Ito, and K. Tanaka, VUV-optical oscillator strength distributions of C_2H_6O and C_3H_8O isomers, J. Chem. Phys. **85**, 4276 (1986).

[30] F. McGrath, A. S. Johnson, D. R. Austin, P. Hawkins, D. Wood, L. Miseikis, E. R. Simpson, M. Castillejo, R. Torres, S. Parker, T. Siegel, and J. P. Marangos, An apparatus for quantitative high-harmonic generation spectroscopy in molecular vapours, Rev. Sci. Instrum. **88**, 103108 (2017).

[31] P. Rudawski, A. Harth, C. Guo, E. Lorek, M. Miranda, C. M. Heyl, W. Larsen, J. Ahrens, O. Prochnow, T. Binhammer, U. Morgner, J. Mauritsson, A. L'Huillier, and C. L. Arnold, Carrier-envelope phase dependent high-order harmonic generation with a high-repetition rate OPCPA-system, Eur. Phys. J. D **69**, 70 (2015).

[32] T. Witting, S. J. Weber, J. W. G. Tisch, and J. P. Marangos, Spatio-temporal characterization of mid-infrared laser pulses with spatially encoded spectral shearing interferometry, Opt. Express **20**, 27974 (2012).

[33] K. R. Kafka, G. Talisa, Noah Tempea, D. R. Austin, C. Neacsu, and E. A. Chowdhury, Few-cycle pulse laser induced damage threshold determination of ultra-broadband optics, Opt. Express **24**, 28858 (2016).

[34] D. R. Austin, K. R. P. Kafka, Y. H. Lai, Z. Wang, C. I. Blaga, and E. A. Chowdhury, Femtosecond laser damage of germanium from near- to mid-infrared wavelengths, Opt. Lett. **43**, 3702 (2018).

[35] M. Lewenstein, P. Balcou, M. Ivanov, A. L'Huillier, and P. B. Corkum, Theory of high-order harmonic generation by low-frequency laser fields, Phys. Rev. A **49**, 2117 (1994).

[36] A. S. Johnson, D. R. Austin, D. A. Wood, C. Brahms, A. Gregory, K. B. Holzner, S. Jarosch, E. W. Larsen, S. Parker, C. S. Strüber, P. Ye, J. W. G. Tisch, and J. P. Marangos, High-flux soft x-ray harmonic generation from ionization-shaped few-cycle laser pulses, Sci. Adv. **4**, eaar3761 (2018); **4**, eaau4713 (2018); **6**, eabc5176 (2020).

[37] M. V. Ammosov, N. B. Delone, and V. P. Krainov, Tunnel ionization of complex atoms and of atomic ions in an alternating electromagnetic field, Zh. Eksp. Teor. Fiz. **91**, 2008 (1986) [Sov. Phys. JETP **64**, 1191 (1986)].

[38] M. Y. Ivanov, M. Spanner, and O. Smirnova, Anatomy of strong field ionization, J. Mod. Opt. **52**, 165 (2005).

[39] M. Bettega, C. Winstead, V. McKoy, A. Jo, A. Gauf, J. Tanner, L. Hargreaves, and M. Khakoo, Collisions of low-energy electrons with isopropanol, Phys. Rev. A **84**, 042702 (2011).

[40] G. Boyle, R. McEachran, D. Cocks, M. Brunger, S. Buckman, S. Dujko, and R. White, *Ab initio* electron scattering cross-sections and transport in liquid xenon, J. Phys. D: Appl. Phys. **49**, 355201 (2016).

[41] M. Michaud, A. Wen, and L. Sanche, Cross sections for low-energy (1–100 eV) electron elastic and inelastic scattering in amorphous ice, Radiat. Res. **159**, 3 (2003).

[42] B. Schütte, P. Ye, S. Patchkovskii, D. R. Austin, C. Brahms, C. Strüber, T. Witting, M. Y. Ivanov, J. W. Tisch, and J. P. Marangos, Strong-field ionization of clusters using two-cycle pulses at 1.8 μm, Sci. Rep. **6**, 39664 (2016).

[43] G. Massillon-JL, Future directions on low-energy radiation dosimetry, Sci. Rep. **11**, 10569 (2021).

[44] W. D. Newhauser, A. B. de Gonzalez, R. Schulte, and C. Lee, A review of radiotherapy-induced late effects research after advanced technology treatments, Front. Oncol. **6**, 13 (2016).

[45] B. Boudaïffa, P. Cloutier, D. Hunting, M. A. Huels, and L. Sanche, Resonant formation of dna strand breaks by low-energy (3 to 20 eV) electrons, Science **287**, 1658 (2000).

[46] M. Rezaee, R. P. Hill, and D. A. Jaffray, The exploitation of low-energy electrons in cancer treatment, Radiat. Res. **188**, 123 (2017).

[47] P. Heissler, E. Lugovoy, R. Hörlein, L. Waldecker, J. Wenz, M. Heigoldt, K. Khrennikov, S. Karsch, F. Krausz, B. Abel, and G. D. Tsakiris, Using the third state of matter: high harmonic generation from liquid targets, New J. Phys. **16**, 113045 (2014).

[48] G. Wyllie, Evaporation and surface structure of liquids, Proc. R. Soc. London A **197**, 383 (1949).

[49] R. Hołyst, M. Litniewski, and D. Jakubczyk, A molecular dynamics test of the Hertz-Knudsen equation for evaporating liquids, Soft Matter **11**, 7201 (2015).

[50] E. Sani and A. Dell'Oro, Spectral optical constants of ethanol and isopropanol from ultraviolet to far infrared, Opt. Mater. (Amsterdam) **60**, 137 (2016).

[51] T. R. Marrero and E. A. Mason, Gaseous diffusion coefficients, J. Phys. Chem. Ref. Data **1**, 3 (1972).

[52] F. McGrath, P. Hawkins, E. Simpson, T. Siegel, Z. Diveki, D. Austin, A. Zair, M. Castillejo, and J. P. Marangos, Extending HHG spectroscopy to new molecular species, in *Ultrafast Phenomena and Nanophotonics XVIII*, Proceedings of SPIE Vol. 8984, edited by M. Betz, A. Y. Elezzabi, J.-J. Song, and K.-T. Tsen (SPIE, Bellingham, WA, 2014), p. 89841B.

[53] C. A. Haworth, L. E. Chipperfield, J. S. Robinson, P. L. Knight, J. P. Marangos, and J. W. G. Tisch, Half-cycle cutoffs in harmonic spectra and robust carrier-envelope phase retrieval, Nat. Phys. **3**, 52 (2007).

[54] A. Shiner, C. Trallero-Herrero, N. Kajumba, B. Schmidt, J. Bertrand, K. T. Kim, H.-C. Bandulet, D. Comtois, J.-C. Kieffer, D. Rayner, P. B. Corkum, F. Légaré, and D. M. Villeneuve, High harmonic cutoff energy scaling and laser intensity measurement with a 1.8 μm laser source, J. Mod. Opt. **60**, 1458 (2013).

[55] B. D. Bruner, M. Krüger, O. Pedatzur, G. Orenstein, D. Azoury, and N. Dudovich, Robust enhancement of high harmonic generation via attosecond control of ionization, Opt. Express **26**, 9310 (2018).

[56] Y. S. You, D. A. Reis, and S. Ghimire, Anisotropic high-harmonic generation in bulk crystals, Nat. Phys. **13**, 345 (2017).

[57] T. Hammond, G. G. Brown, K. T. Kim, D. Villeneuve, and P. Corkum, Attosecond pulses measured from the attosecond lighthouse, Nat. Photonics **10**, 171 (2016).